

SI Appendix

Supporting Materials (references cited here can be found in the reference list in the main text):

SupplementaryText
Figs. S1 to S13
Table S1
Captions for Supporting Movies S1 to S5

Other Supporting Materials for this manuscript includes the following:

Movies S1 to S5

Supporting Figures S1 – S13

Introduction

The core discovery of this work is the fast and reversible formation of transient connexin depleted regions (tCDRs) induced by AB5 toxins within gap junction (GJ) plaques. Formation of tCDRs has not been described before and, more importantly, represents the first record of a generalized response of the entire GJ plaque to bacterial pathogens with AB5 structure. tCDR formation was first observed during live cell analysis of GJ plaques with spinning disk confocal microscopy and further resolved using Bessel Beam plane illumination microscopy (Planchon et al., 2011) over time. Using Bessel beam plane illumination microscopy we imaged how tCDRs progress through the entire 3D space of the GJ plaque, most likely inducing membrane re-arrangements of connexin clusters within the GJ plaques. We used this non-diffracting super-resolution technique, because it is well suited for the curved GJ membrane domains. These combined microscopy approaches enabled us to assess tCDR responses of GJ plaques composed of different connexin isoforms, namely Cx30, Cx36, Cx43, and Cx45. Formation of tCDRs was recorded in a real 3D space of naturally tilted cell-cell contacts as shown in Fig. S1. GJ plaques (typically several μm in extent) were visualized from different angles depending on the orientation of membranes between the contacting cells. We suggest that fast, millisecond range formation of tCDRs which proceeds via toxin-induced plasma membrane binding of gangliosides / globotriaosylceramide reflects lipid rearrangements of the membrane, resulting in changes of the packing of connexin channel clusters within the GJ plaque.

Figures:

- Fig. S1. Optical configuration of Bessel Beam setup used for GJ analyses*
- Fig. S2. Time-resolved tCDR formation*
- Fig. S3. Chemically induced stationary CDRs*
- Fig. S4. Actin cytoskeleton and tCDR dynamics*
- Fig. S5. Dual patch clamp electrophysiology analyses*
- Fig. S6. Absence of co-localization between tCDRs and AB5 toxins in GJ plaques*
- Fig. S7. Formation of tCDRs and Ca^{2+} responses*
- Fig. S8. Optosplit configuration for live cell FRET analyses*
- Fig. S9. cAMP measurements using Optosplit FRET*
- Fig. S10. cAMP changes induced by 8-Bromo-cAMP*
- Fig. S11. cAMP profile in CTX treated cells*
- Fig. S12. cAMP oscillations between GJ coupled cells*
- Fig. S13. Absence of tCDR formation in filipin - treated cells*

Fig. S1

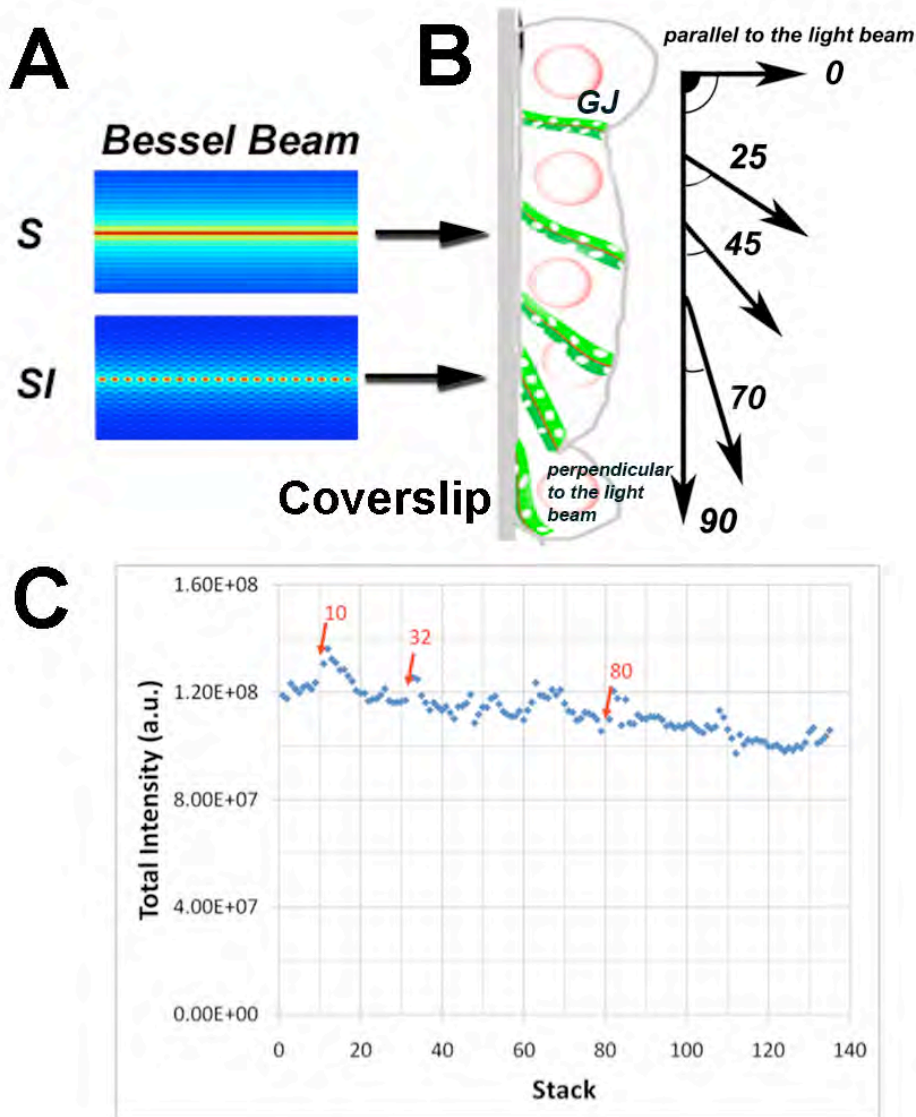


Fig. S1: Optical configuration of the Bessel Beam plane illumination microscope setup

(A) A schematic view of the Bessel beam operating in a horizontal position (whereas coverslips with cell monolayers are in a vertical position (grey bar in B)). The advantage of a vertical coverslip orientation allowed us to use g-force for the fast application and removal of bacterial toxins.

(B) GJ plaques are naturally tilted between cell-cell contacts. Different positions of GJ plaques towards the Bessel beam are indicated as angles. Bessel beam plane illumination microscopy allows obtaining sub-diffraction resolution along axes as follows: X-180 nm / Y-180 nm / Z-300 nm in the one-photon imaging mode, and near isotropic 3D resolution at ~300 nm (along the X, Y and Z axes) in the two-photon mode (Planchon et al., 2011).

(C) Integrated intensity fluctuations through the data stack. Original data were obtained with Bessel Beam plane illumination microscopy and correspond to the data set shown in Movie S1. Here we plotted integrated intensity fluctuations for each stack along the Y-axis with the time of acquired image in stack along the X-axis (5 seconds interval between stacks; see movie S2). Red arrows above the plotted data indicate moments when toxins were added. Numbers on the X-axis correspond to the sequential stack numbers acquired during the imaging experiment. Note that the integrated total fluorescence of the entire GJ plaque showed only minimal changes upon AB5 toxin applications and tCDR formation and recovery. During the course of the experiment a slow, steady decline in total fluorescence is observed, probably due to photobleaching.

Fig. S2

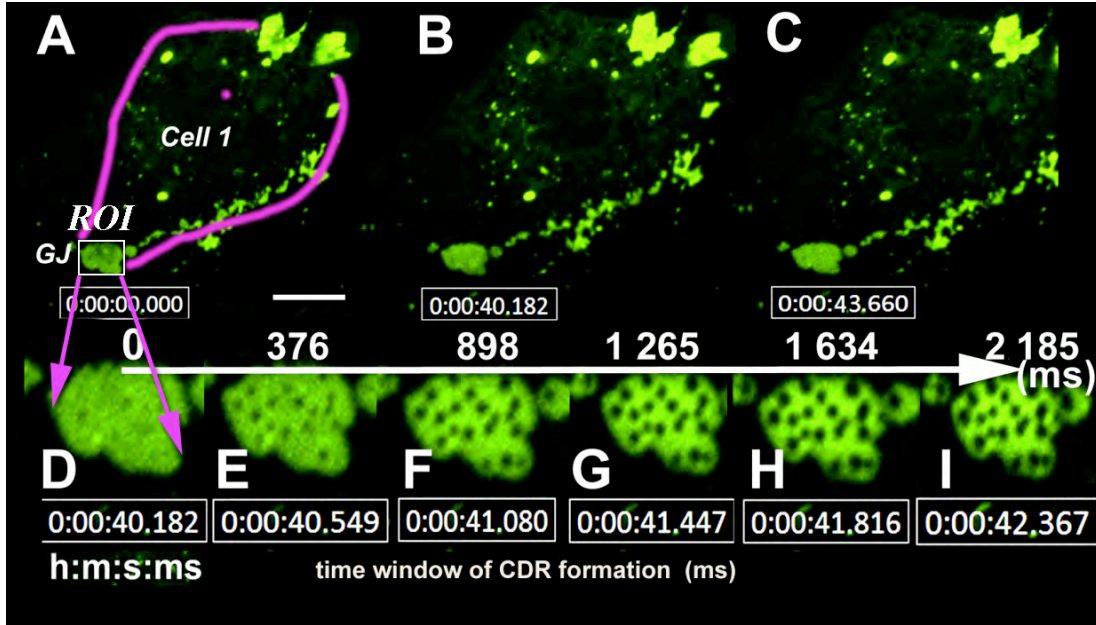


Fig. S2: Time-resolved tCDR formation.

In an attempt to resolve the fast kinetics of tCDR formation in real time we acquired images at free-run speed of an Andor EM-CCD camera fitted to a spinning disk confocal microscope. The acquisition software displayed the resulting time interval between individual frames as between 376 – 551 milliseconds (see the corresponding movie S5).

(A - I) Appearance of first tCDRs following CTX application can be detected in frames D and E, while the process is near complete in F. Only Cell-1 (out of 3 cells forming two GJ contacts) is outlined in pink. Actual times of image acquisition are indicated below individual frames as: /hours: minutes: seconds: milliseconds/.

(D - I) tCDRs in the process of formation recorded in *en-face* view. A higher magnification of the ROI within the GJ plaque (indicated by a white box) in (A) is shown. Calculated times (in milliseconds) of tCDR formation are indicated. tCDR formation is at maximal extent at 2185 milliseconds after the beginning of the process, or even earlier. Very similar kinetic data for tCDR formation ranging from 0.9 to 2.5 seconds were obtained in experiments with other AB5 toxins as listed in Table S1.

Fig. S3

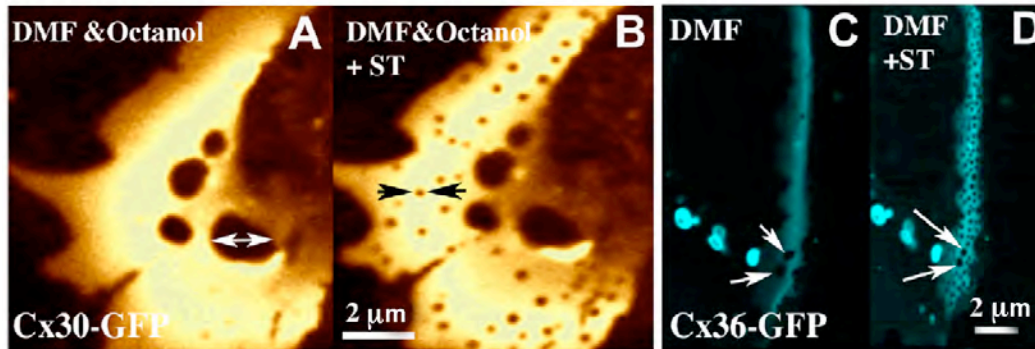


Fig. S3: Long-lived, stationary CDRs can be induced by different chemical agents. (A) GJ plaques between Vero cells expressing Cx30-EGFP develop long-lived CDRs as a result of treatment with a mixture of DMF (dimethylformamide) and octanol (1%/1% [V/V]). Note the presence of large non-fluorescent areas (stationary CDRs) inside the Cx30-EGFP GJ plaque after addition of DMF/Octanol (one marked by white arrows). (B) Application of STx1 to a GJ plaque already containing chemically induced long-lived CDRs (A) immediately resulted in toxin-induced CDRs (black arrows) that were 10 - 100 times smaller in area than the chemically induced CDRs. (C-D) Example of a Cx36-EGFP labeled GJ plaque treated with DMF (C) prior to the application of STx1 (D). In contrast to the relatively stable DMF-induced CDRs (white arrows), the smaller STx1 - induced tCDRs were distributed over the entire GJ plaque, revealing a generalized nature of the tCDR-response. [Artificial colors were chosen such as to best display the different types of CDRs].

Table S1: Toxins used in this study and their effects on GJs

AB5 \ Gap junctions	Cx30	Cx36	Cx43	Cx45
wtCTX and CTX-K63	+	+	+	+
wt ST (STx1)	+	+	+	+
wt LT-1	+	+	+	+
STx1-B	+	+	+	+
CTX-B	+	+	+	+
STx2 (EHEC)	+	+	+	+
CNF (not AB5 toxin)	-	-	-	-

Table S1.

Gap junction isoforms and tCDR-response to different AB5 family toxins.

Fluorescently labelled GJ plaques formed from different connexin isoforms expressed in Vero cells used in this study are listed.

Cells forming gap junctions were treated with AB5 toxins as described in the text.

At least 10 GJ plaques each were imaged with different bacterial toxins for each connexin isoform;

(+) indicates that 10 tested GJs responded with tCDR formation (100%).

(-) indicates that 10 tested GJs did not respond with tCDR formation.

Fig. S4

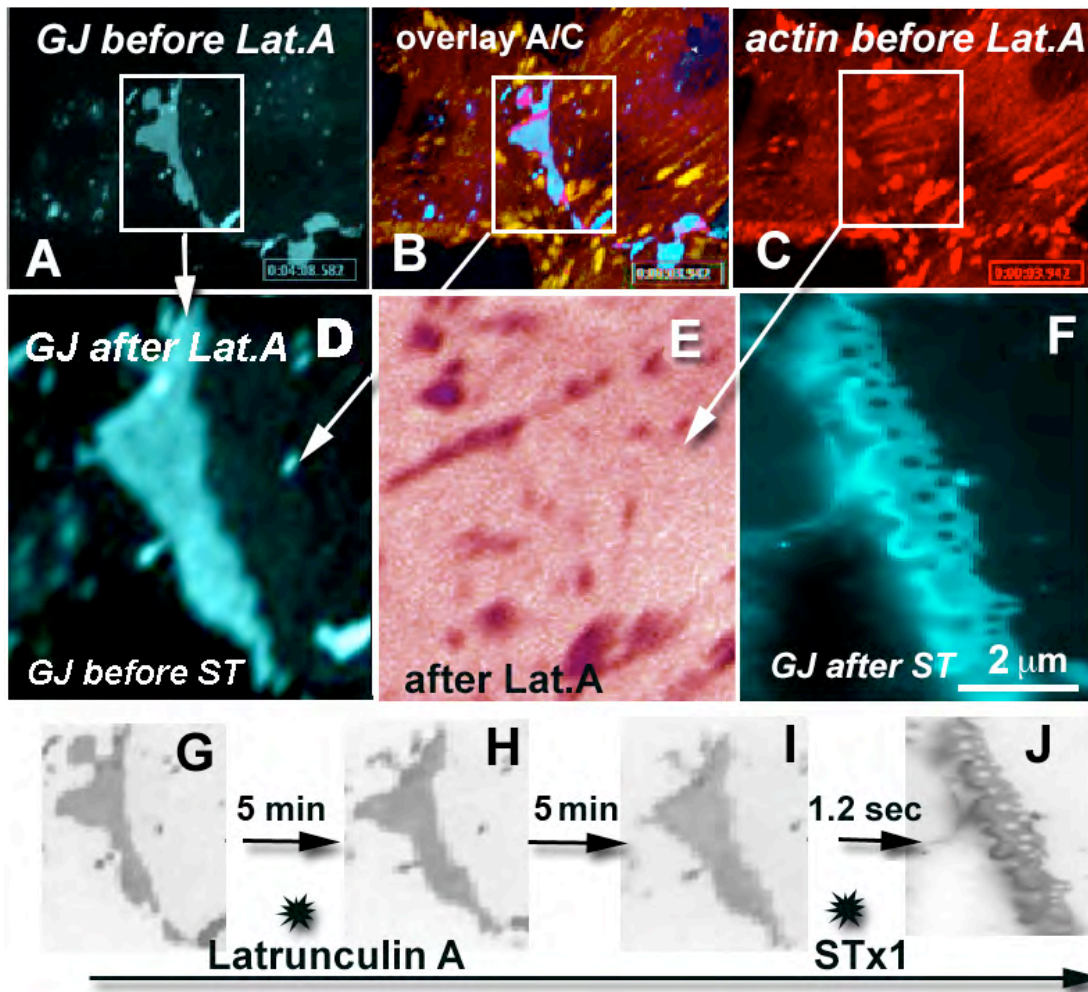


Fig. S4. Disruption of the actin cytoskeleton does not affect AB5 toxin-induced formation of tCDRs.

(A-C) Cx30-CFP (A), Actin-mRFP (C, red), and a 3-channel overlay of Cx30-CFP and Actin-mRFP that includes the actin-binding protein Zyxin-YFP (B). All three FP-tagged proteins were co-expressed in Vero cells.

(D, E) Magnification of the ROI indicated with a white box and arrows in (A-C). (E) In Latrunculin A treated cells (10 μM final conc.; 10 min) actin stress fiber fluorescence disappeared. (F) Nevertheless, STx1 induced formation of tCDRs with similar kinetics (F) compared to control cells.

(G-J) Addition of Latrunculin (asterisk on the left) caused only small shape changes of the GJ plaque over a time course: 0 min (G), 5 min (H), and 10 min (I) after addition of the drug. (J) Addition of STx1 (asterisk on the right) rapidly induced tCDRs. Note that in the absence of actin filaments the GJ plaque changes shape rapidly and dramatically in response to STx1. Contrast-inverted images of the Cx30-EGFP fluorescence are shown in (G-J).

Fig. S5

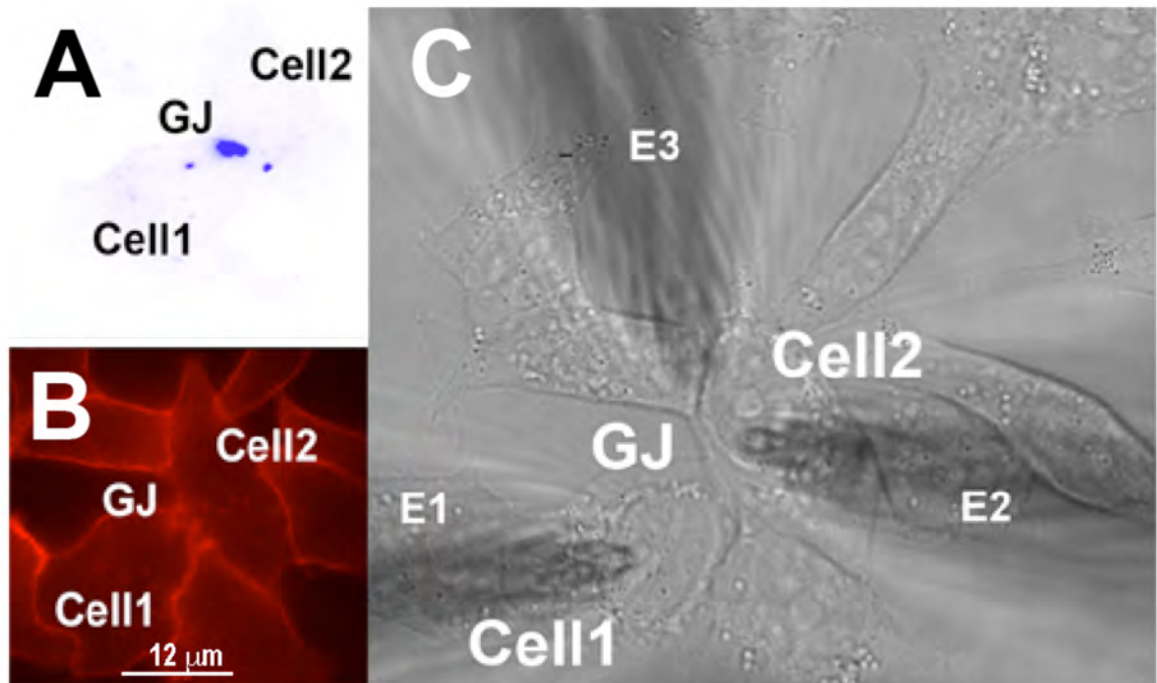


Fig. S5: Dual patch clamp electrophysiology recordings of cell-cell contact during tCDR formation.

(A) Two cells Cell1 and Cell2 forming a GJ plaque (Cx36-GJ) [a contrast-inverted image of the Cx36-EGFP fluorescence is shown].

(B) After application of fluorescently labelled CTX labelling at the PM can be seen.

(C) DIC image of 3 cells with recording electrodes; dual patch clamp setup (Electrode E1 and E2). The electrophysiology results are shown in Fig. 2D in the main text.

Fig. S6

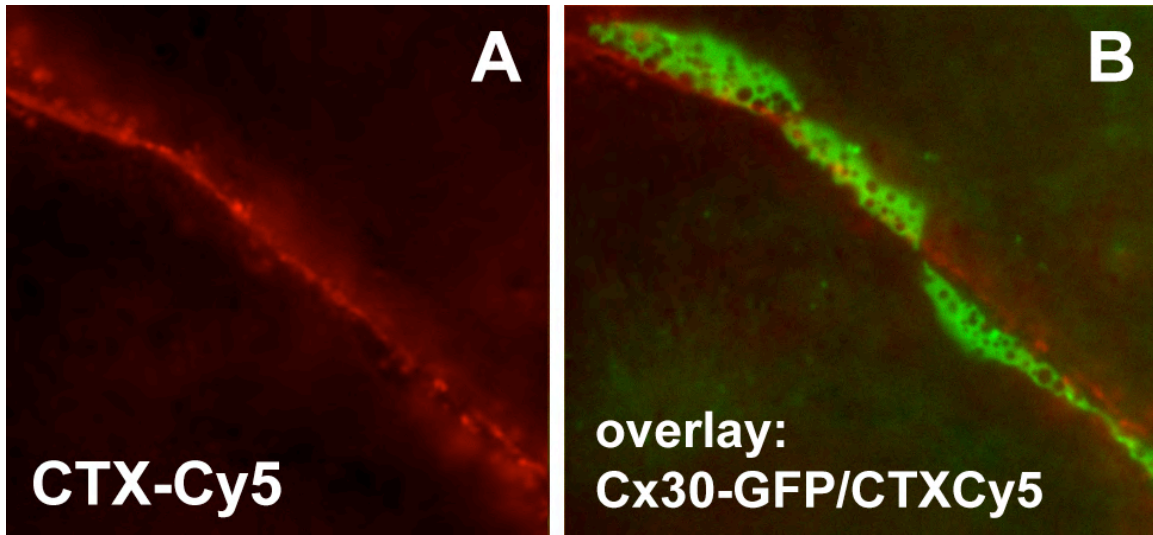


Fig. S6. Absence of co-localization between toxin-induced tCDRs and cholera toxin within the GJ plaque.

(A) Cell-cell contact interface revealed Cy5-labeled CTX at the plasma membrane.

(B) Dual color image overlay of CTX-Cy5 and Cx30-EGFP. Note that the tCDRs formed inside the Cx30-EGFP labelled GJ plaque do not colocalize with fluorescence of the applied toxin, supporting the idea that toxin-induced tCDRs appeared as a generalized response of the entire GJ plaque to AB5 toxins and are not “holes” physically induced by toxins inside the GJ plaque.

Fig. S7

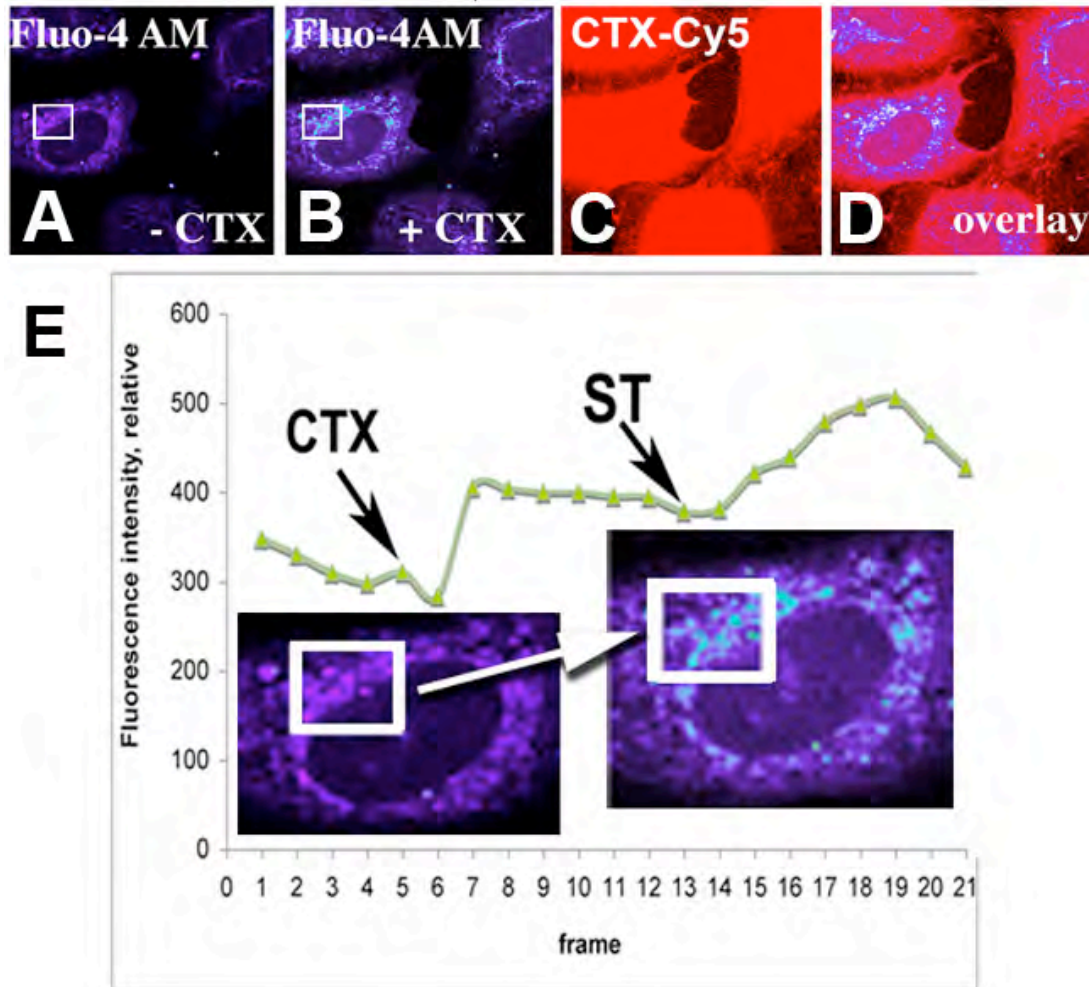


Fig. S7. Application of Cholera and Shiga toxins induce Ca^{2+} responses measurable with Fluo-4 AM.

(A, B) Vero cells before and after application of CTX. Maximum, minimum and integrated values of the Fluo-4 AM calcium sensor fluorescence intensity within selected ROI (white squares enlarged in E) over the stack of images were obtained with the MetaMorph 7.6 program. Integrated relative fluorescence is plotted in (E) (C, D) Cy5-labelled CTX was visualized by spinning disk microscopy; an overlay of (B) and (C) is shown in (D).

(E) Time course of $[\text{Ca}^{2+}]_i$ levels in cells measured using Fluo-4 AM fluorescence, before and after application of CTX and STx1 (arrows). Original fluorescence microscopy data are presented as 2 inserts, corresponding to frames 5 and 10 of the time sequence. Note a visible fluorescence increase in the region of interest after CTX addition (white box). Image acquisition time used was 800 milliseconds, and the interval between frames was 2.5 seconds. In mammalian cells, intracellular free calcium levels are typically below 100 nM. In CTX - treated cells the measured calcium varied from $\approx 800\text{-}500$ nM at the center of cells and around the nuclear envelope (presumably in the ER regions as well) while decreasing to $\approx 400\text{-}300$ nM in sub-plasma membrane regions. That means that the transient CTX - induced calcium level was up-regulated 4-7 fold compared to non-treated cells. Temporary increases of intracellular Ca^{2+} caused by treatment of cells with the B subunit of CTX has been described (Milani et al., 1992). Further, elevation of intracellular Ca^{2+} levels in response to STx1 induced ER stress and increased Ca^{2+} release from ER stores into the cytoplasm has also been reported (Lee et al., 2008). Toxin-induced transient increase of $[\text{Ca}^{2+}]_i$ level to this degree is known to initiate dramatic changes in the cellular metabolism, possibly as a part of an orchestrated host response program towards bacterial pathogens. To tolerate this high level of $[\text{Ca}^{2+}]_i$ cells should increase membrane transport of Ca^{2+} out of cells by activating the calcium-ATPase to facilitate Na/Ca exchange.

Fig. S8

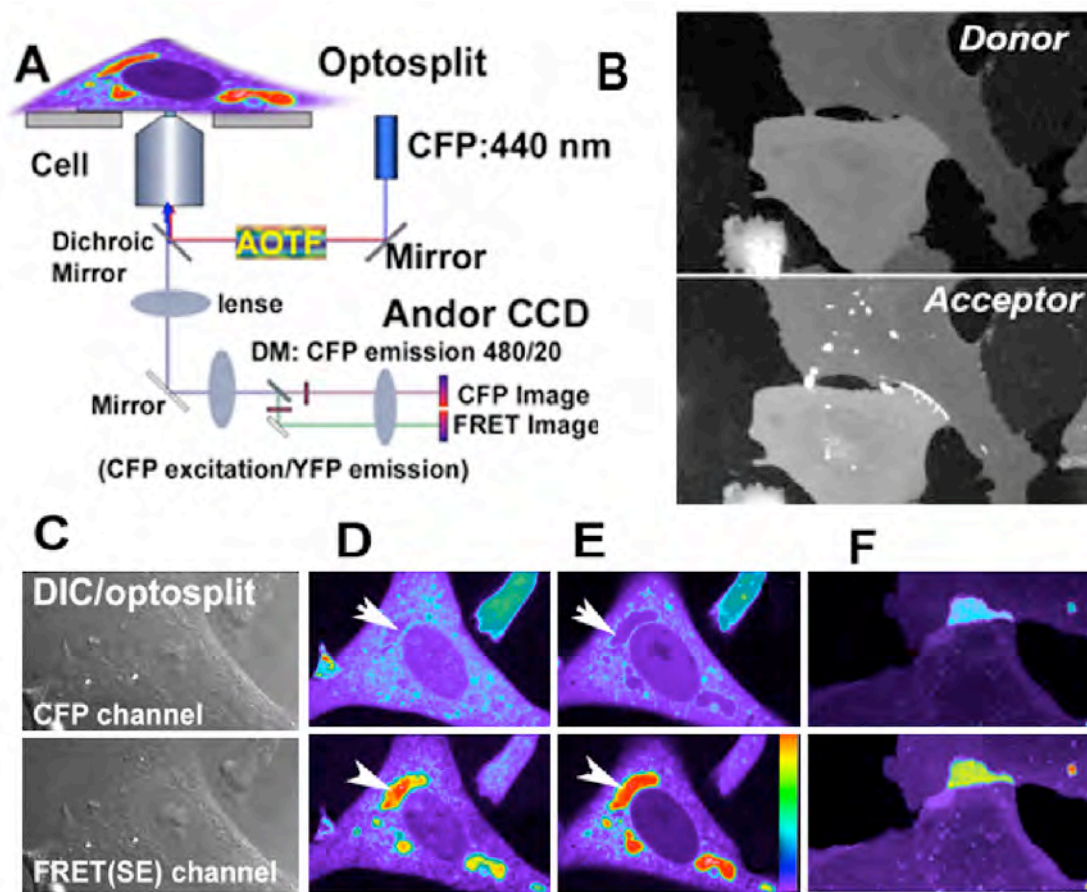


Fig. S8. Optosplit configuration for fast detection of FRET.

(A) Simultaneous dual CFP/YFP image acquisition using a Spinning-Disk-Optosplit combo system. Precise separation of light by the dichroic mirror was followed by the adjustment of two light projections from the same cell (or cell region) onto the chip of an Andor EM CCD camera. This set-up allowed us to monitor different fluorescent signals of the same cell acquired from two different operating channels and to perform simultaneous image analyses of FRET with proteins expressed as Donor-Acceptor pairs.

(B) Here we demonstrated that under selected filter-sets and excitation minimal cross-talk between Donor (CFP) and Acceptor FRET/YFP channel occurred. In the Acceptor (YFP) -channel expression of Cx30-YFP in the same cells is seen. (C) DIC images of the same cell shown later in (D, E).

(D-E) A CFP/YFP - FRET pair co-expressed in cells was used as a positive control, namely ArfGAP-CFP and KDEL-receptor YFP (described as an excellent FRET control pair earlier by us (Majoul et al., 2001, Majoul, 2006). Donor image (CFP, upper panel) reveals complete depletion of energy that is transferred now to the acceptor molecule (lower panel). Two images representing the same process in the development of FRET. The color table in the lower panel of E indicates changes of FRET efficiency from 0 (blue) to 0.4 (red). (F) Cx43-CFP/Cx43-YFP FRET between connexin molecules forming mixed GJ channels observed using the Optosplit system.

Fig. S9

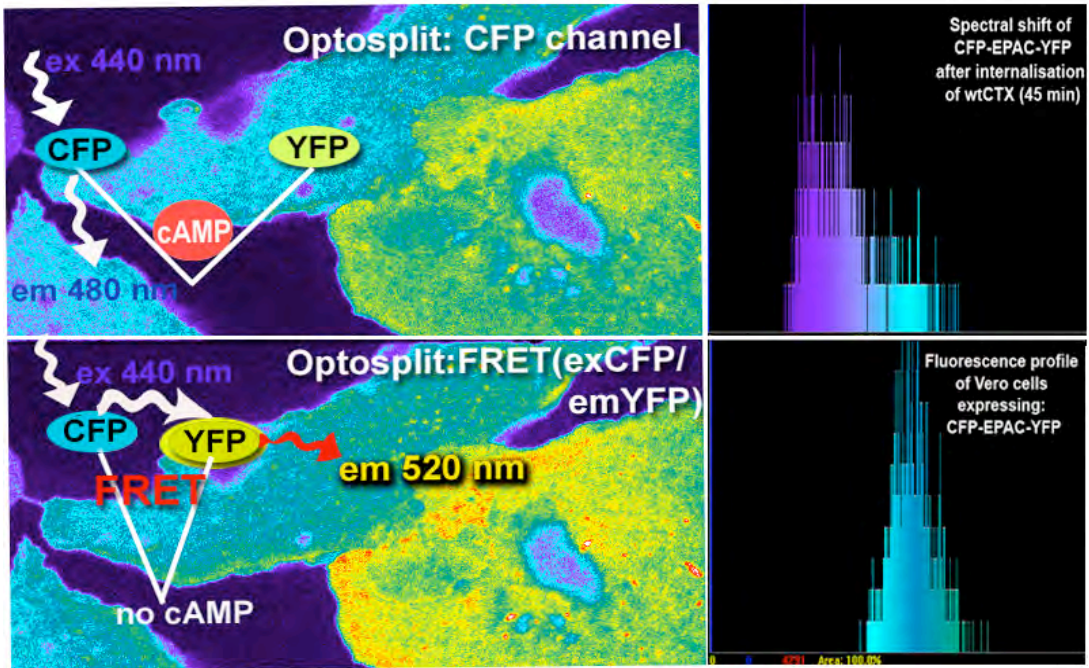


Fig. S9: Principles of FRET-based cAMP measurements using Optosplit – FRET.

(left panel, upper image): Two cells expressing EPAC sensor (the exchange factor is fused between the CFP- and YFP- chromophores and is directly activated by cAMP (Ponsioen et al., 2009; Ponsioen et al., 2004) form GJ contacts. Application of CTX raises cellular cAMP level that was directly measured using this FRET based sensor. cAMP binds to the EPAC domain between CFP and YFP, increasing the FRET distance and resulting in an increased CFP-emission (440 nm).

(left panel, image below): decrease of cAMP level reverses the conformation of EPAC molecule, resulting in close proximity of CFP and YFP and increased FRET, i.e. increased YFP-emission (520 nm).

(right panel): cAMP-dependent histogram of the fluorescence distribution in cells expressing EPAC sensor. Using this system we examined the role of tCDR formation in synchronicity of cAMP levels between GJ - coupled cells.

Fig. S10

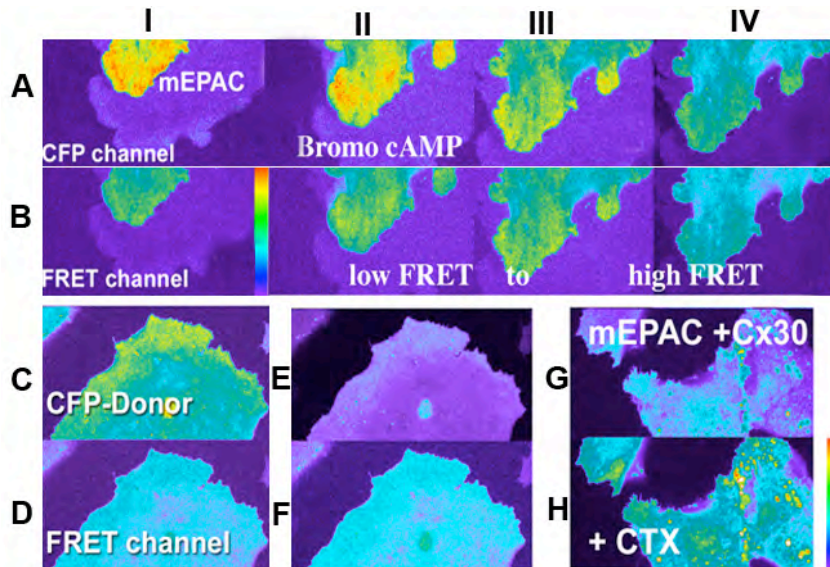


Fig. S10: Modulations of cAMP level measured in living cells.

(A-B) The EPAC sensor expressed in Vero cells reveals moderate FRET. Because cAMP is an extremely short-lived molecule, we added 8-Bromo-cAMP (a slowly hydrolysable cAMP analog) to cells in order to decrease FRET values. The time-dependent decrease of cAMP level is reflected by an increase in donor-acceptor FRET (stage IV).

(C-D, E-F) Cholera toxin treatment induced cAMP fluctuations.

(G-H) Cells linked by GJ contacts showed synchronicity in cAMP induced FRET. Two selected regions of interest were measured in two cells connected via GJs.

Fig. S11

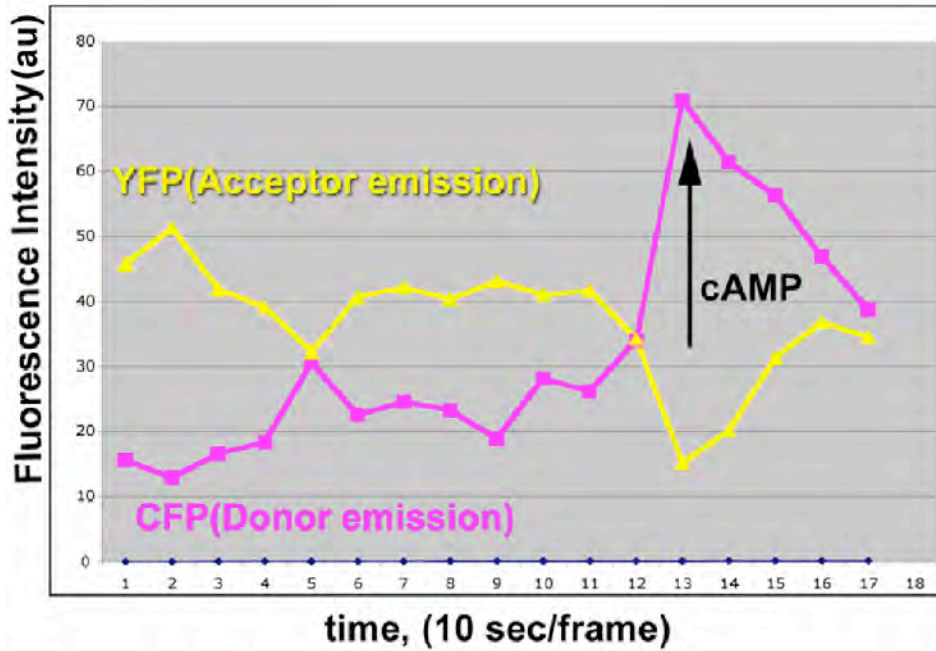
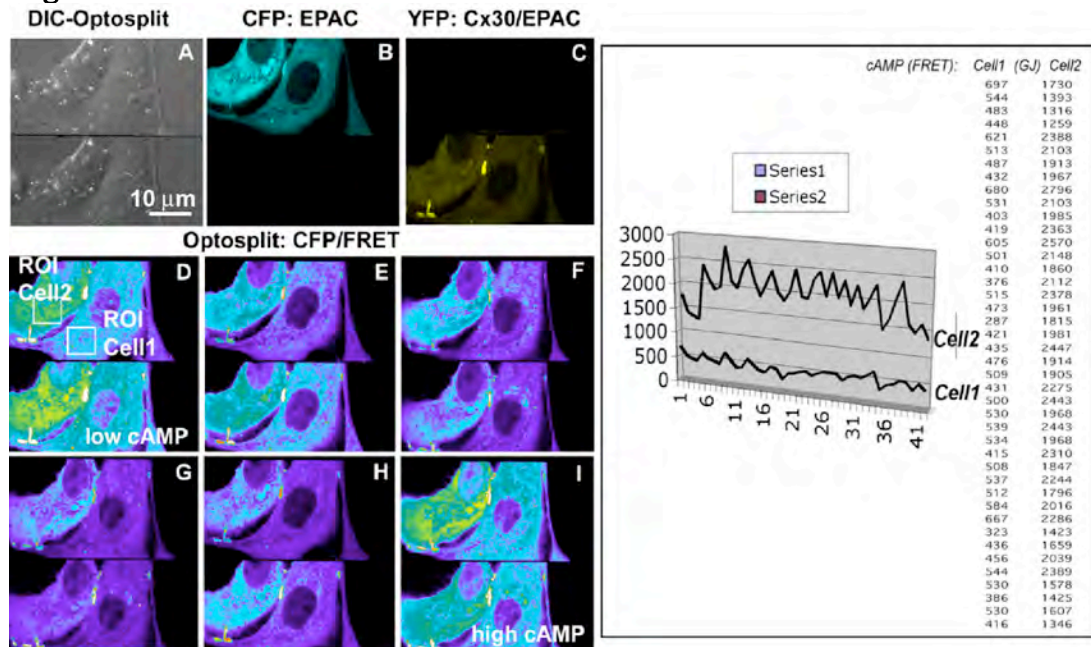


Fig. S11. cAMP profile in cells treated with wild-type CTX

Previously we demonstrated that cholera toxin induces a strong increase in cAMP, up to 17-20-fold compared to background levels (Majoul et al., 1996). Here, using an Optosplit setup and the CFP-YFP-encoded FRET-based cAMP sensor EPAC we show that much smaller but repeatable cAMP fluctuations spontaneously appeared and disappeared upon cholera toxin treatment. Such fluctuations were not observed when only the pentameric CTX B-subunit was used (data not shown).

Fig. S12**Fig. S12: Synchronous cAMP oscillations between GJ - coupled cells**

(A). DIC image of two contacting cells taken through the Optosplit system. Cells were transfected with cAMP EPAC sensor and Cx30-YFP.

(B) Image of the same cells taken through the Optosplit system with CFP filters only. (For a reference on the Optosplit system see Fig. S8). The CFP channel revealed mainly the cellular distribution of EPAC sensor; note that both cells are transfected.

(C) Image of two contacting cells taken via Optosplit upon YFP-laser excitation through a narrow band pass YFP filter set revealed absence of contaminating signal in the CFP half-channel and low background YFP fluorescence in the cytoplasm of both cells. Strong appearance of Cx30-YFP fluorescence at the cell-cell contact interface showed that the two cells are linked by gap junctions.

(D-I) Selected time-frames of EPAC fluorescence in both cells taken with the Optosplit system upon CFP excitation and with FRET emission filters. To measure cAMP fluctuations in time between two cells signals from two ROI (Cell 1 and Cell 2) were selected. Original data from two ROI are shown on the right panel. cAMP fluctuations in GJ coupled cells can be seen in the common graph for both Cells 1 and Cell2 over time. Scale bar 10 μ m.

Optosplit FRET measurements present additional parameters concerning the intracellular measurements of intensity fluctuations inside the GJ plaque during tCDR formation. Two cells co-expressing EPAC sensor and forming GJ (Cx30-YFP) contacts were imaged before, during and after CTX treatment. Intensity fluctuations of EPAC-FRET in selected regions of interest inside the coupled cells were analyzed over time. As cAMP is a very short-lived molecule and cellular phosphodiesterases may cleave cAMP faster than we would be able to image the process, we did not expect significant changes. Nevertheless, the obtained data presented as a diagram below revealed that cells which form functional GJs operate in synchrony to support a “frequency encoded second messenger system” (Berridge, 2006). GJ linked cells are known to transfer Ca^{2+} via GJ channels along the electrochemical gradient by diffusion, but Cx30 and Cx36 gap junctions were described as ‘low-pass’ channels (Galarreta and Hestrin, 2001) with weak voltage dependence (Srinivas et al., 1999) and overall small channel conductance (White and Paul, 1999). In contrast, Cx36 was suggested to be important for exchange of second messengers such as cAMP, nitric oxide and dopamine, which are known to modulate gap junctional conductivity of cells (Mills and Massey, 1995) (Xin and Bloomfield, 2000). Cx36 associated proteins were found to be phosphorylated in response to cAMP (Sitaramayya et al., 2003) and the diffusion of dye in cells expressing Cx35 is modulated by PKA (O'Brien et al., 2004). Therefore, cAMP waves are of paramount importance at the cellular and molecular level where signalling is finely tuned (Leybaert et al., 1998; Saez et al., 1989; Sneyd et al., 1998). Two cells forming a GJ contact and expressing EPAC cAMP sensor are shown. cAMP was measured before, during and after application of toxin. Selected regions of interest were defined and used to calculate the corresponding changes in cAMP level between Cell1 and Cell2 that are connected via the Cx30-YFP labelled GJ plaques.

Fig. S13

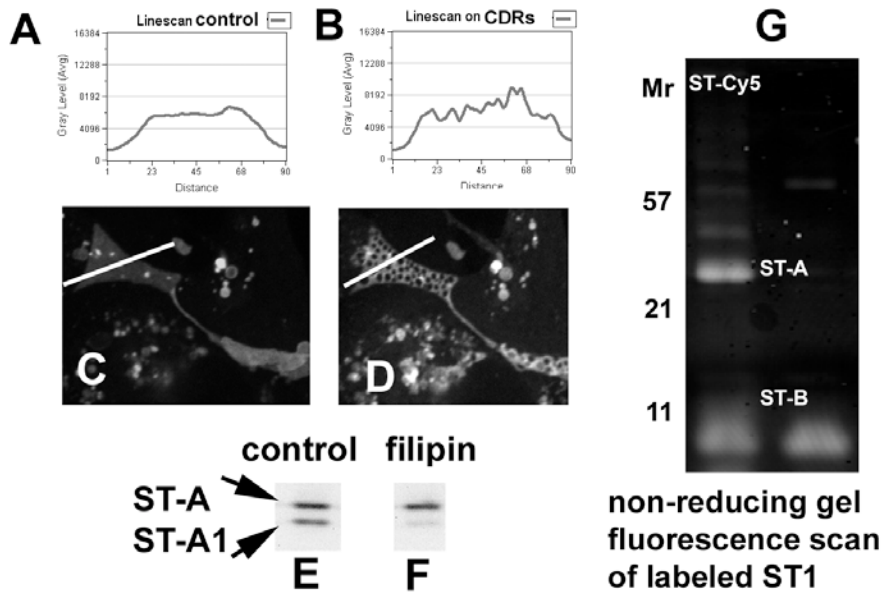


Fig. S13: Absence of tCDR responses to STx1 in filipin-treated cells.

Filipin treatment not only prevents formation of tCDRs, but also strongly decreases the correct processing of AB5 toxins in the cell.

(A and B) Intensity line scan before and during tCDR formation (corresponding to the fluorescence images shown in C and D [the white bar indicates the line scan region of interest in the cell]).

(D) Image of tCDRs of cells under low toxin/high K⁺ conditions (as in Fig.4).

(E and F) processing of STx1 in Vero cells 1.5 hrs after internalization: E - in control, F-in filipin treated cells (10 µg/ml). Note reduced processing of the STx1 A-subunit into A1 in filipin – treated cells.

(G) Purified Cy5 - labelled STx1 holotoxin resolved on a non-reducing 12% SDS polyacrylamide gel. Note preferential labelling of either both the A and B subunits, or B alone, achieved under different pH conditions of the Bicine buffer.

Captions for supplemental movies S1 - S5

Movie S1.

tCDR formation resolved by Bessel Beam plane illumination microscopy, A 3D projection of a gap junction plaque labelled with Cx30-EGFP from different viewing angles is shown. Note the presence of motile sub-structures clearly visualized within the GJ plaque that may represent clusters of connexin channels. The GJ plaque repeatedly responded to the application of CTX (3 times) and STx1 (2 times). Note the fast formation and recovery of multiple tCDRs in response to both AB5 toxins. 207 3D image stacks were acquired every 20 seconds (i.e. a total observation time of 69 min), and are shown in the time lapse movie at 12 frames / second (i.e. at ~240x real speed). Selected frames are also shown in Fig. 1. Stack numbers and a time stamp are shown in the upper right corner.

During the entire image acquisition only minimal fluctuations of total integrated fluorescence intensity of the 3D stack were observed (see Fig. S1 C). However, a slow, steady decrease of total integrated fluorescence over the course of the experiment is apparent, most likely due to photobleaching (Fig. S1 C).

Movie S2.

Dynamic 3D resolution of tCDR formation in a Cx30-EGFP labeled GJ plaque induced by shiga toxin (selected frames from this movie are shown in Fig. 2). The left panel shows an *en-face* view of the GJ plaque, and the right panel a side view of the GJ plaque from the 4D stack. Stationary CDRs (which in Fig. 2 B and C are indicated by violet arrows) recover back towards the end of the movie. Note that during tCDR formation and recovery the 3D outline, geometry and size of the GJ plaque does not change very much. Note that rapid formation and slower disappearance of tCDRs both occur much faster than the movement of Cx30-EGFP containing membrane structures (right panel). For this movie, 134 3-D image stacks were acquired at 5 second intervals by two-photon mode Bessel beam plane illumination microscopy. The total time sequence represents 442 seconds and is displayed at 11 frames / second, i. e. at 36x real speed.

Movie S3.

Rotation (of a 3D rendering) of selected image stacks (stacks 8, 10, 30, and 32) taken from movie S2, showing the same GJ plaque before and after tCDR formation (image stacks 8 and 10, and 30 and 32 document the tCDR response of the same GJ plaque to two pulses of STx1). Note two stationary CDRs in stacks 8 and 30 at the same positions before and after tCDR recovery. Also note that tCDR formation in response to the two pulses of STx1 occurs at different positions within the GJ plaque. Times are indicated in seconds.

Movie S4.

CDR formation in a Cx30-CFP labelled GJ plaque imaged using spinning disk confocal microscopy. Note the repeated, reversible tCDR formation in response to two pulses of CTX (added at time points 10 min, and 24 min, respectively) and one pulse of shiga toxin (added at 23 min). This corresponds to selected frames A-E, G-K, and N-R in Fig. 3 in the main text. Further note the smooth fluorescence of the GJ plaque (i.e. the absence of any visible substructures) in contrast to the movies S1 - S3 which were acquired using Bessel beam plane illumination microscopy. The total time sequence shown corresponds to 6 hours and 9 minutes. Time-lapse images were taken every 15 seconds, and are shown at 200x real speed. At time point 32 min, i.e. after tCDR recovery from three pulses of AB5 toxins, irreversible structural alterations in the GJ plaque were starting and were accompanied by slow internalization of the GJ plaque over the next 5.5 hours of observation. During the last 4 hours of the movie acquisition rate was slower, 1 frame / 2 min. Times are indicated in the time stamp box as hrs:min:sec:milliseconds.

Movie S5.

The kinetics of tCDR formation recorded using a fast, free-run image acquisition with an Andor EM-CCD camera (with ~376 ms / frame). Note the very fast appearance of tCDRs within a time interval of 700 - 800 milliseconds. The movie corresponds to the selected frames shown in fig. S2 A-I, but represents a larger ROI than the one shown in Fig. S2 D - I.